Synchronized states of hydrodynamically coupled filaments and their stability

Smitha Maretvadakethope[*]

Department of Mathematical Sciences

University of Liverpool

Mathematical Sciences Building

LIVERPOOL

L69 7ZL

UK

Yongyun Hwang[†]

Department of Aeronautics

Imperial College London

South Kensington Campus

LONDON

SW7 2AZ

UK

Eric E Keaveny[‡]

Department of Mathematics

Imperial College London

South Kensington Campus

LONDON

SW7 2AZ

UK

(Dated: May 5, 2022)

Abstract

Cilia and flagella are organelles that play central roles in unicellular locomotion, embryonic development, and fluid transport around tissues. In these examples, multiple cilia are often found in close proximity and exhibit coordinated motion. Inspired by the flagellar motion of biflagellate cells, we examine the synchrony exhibited by a filament pair surrounded by a viscous fluid and tethered to a rigid planar surface. A geometrically-switching base moment drives filament motion, and we characterize how the stability of synchonized states depends of the base torque magnitude. In particular, we study the emergence of bistability that occurs when the anti-phase, breast-stroke branch becomes unstable. Using a bisection algorithm, we find the unstable edge-state that exists between the two basins of attraction when the system exhibits bistability. We establish a bifurcation diagram, study the nature of the bifurcation points, and find that the observed dynamical system can be captured by a modified version of Adler's equation. The bifurcation diagram and presence of bistability reveal a simple mechanism by which the anti-phase breast stroke can be modulated, or switched entirely to in-phase undulations through the variation of a single bifurcation parameter.

I. INTRODUCTION

Cilia and eukaryotic flagella [1] are slender, flexible filaments that are used by microorganisms for motility, and by the tissues of larger organisms to facilitate fluid transport. While there are many examples of cells that possess a single flagellum, a prime example being the properly-formed human sperm cell [2], there are many instances where cells are equipped with multiple flagella or cilia. These organisms may use a pair of flagella, as is the case of the unicellular algae *Chlamydomonas* [3], or may have large numbers distributed over their entire surface, as observed for the unicellular *Paramecium* [4] and the multicellular algae colonies, *Volvox* [3]. Fluid motion generated by large groups of cilia are also essential to the proper function of larger organisms where it impacts embryo development [5], the movement of mucus in the lungs [6], and the transport of cerebrospinal fluid in the brain [7].

The movement of a single cilium or flagellum is the result of the relative sliding of microtubule pairs that run the length of the flagellum or cilium and make up the internal

* sm6412@liverpool.ac.uk

† y.hwang@imperial.ac.uk

‡ e.keaveny@imperial.ac.uk

structure known as the axoneme [1]. While the precise details of the force generation along the axoneme remain an active topic of current research, it results in periodic beating that can be viewed as a limit cycle. Key to facilitating transport in systems with multiple cilia is how the motions of individual cilia are coordinated with those of their neighbors. For examples involving large numbers of cilia or flagella, one of the most widely studied forms of coordination is the metachronal wave [4]. With metachronal waves, the interactions between cilia result in a phase shift between their limit cycles that increases linearly with the distance between cilia. Metachronal waves break the time-reversal symmetry [8] associated with viscosity-dominated flows, assisting the asymmetric cilium beat in providing net fluid motion or cell propulsion. Coordination is also paramount when smaller number of flagella are involved. In the case of *Chlamydomonas*, its two flagella are observed to beat predominantly in an anti-phase breast stroke that occurs during forward swimming [9–11]. In-phase, parallel undulations, however, can also be excited [12] when the cell experiences a sudden stimulus and attempts to quickly move away from the source [12, 13].

Multiple physical mechanisms [14] are involved in giving rise to the observed coordinated states. Interactions between neighboring cilia or flagella are mediated through the surrounding fluid [15], or through a more direct coupling at the surface, where the flagella may be connected though compliant structures, as is the case of the distal striated fiber found in the basal body [16, 17] of *Chlamydomonas*. Additionally, the surface may be that of a cell which is free to move in the surrounding fluid, providing a further potential mechanism for coupled motion [18]. The response of the cilia and flagella to mechanical signals can further depend on their internal constitutive properties [19], along with the precise mechanism by which internal force generation is regulated in response to external loads [20].

While many of these effects have been successfully combined in computational models [6, 21, 22] that provide detailed descriptions of individual cilia and their hydrodynamic interactions, elasticity, and internal actuation, simpler models [23] that capture the essence of ciliary systems have been particularly effective in providing insight into coordination. These models have been used successfully in conjunction with experimental studies [24, 25] on model organisms, as well as with physical models [26] of ciliary systems constructed from optical traps and colloidal particles. In these models, the cilia are treated as spherical particles that move along restricted paths and whose hydrodynamic interactions are described by the flow due to a point force (Stokeslet). The phase of the oscillator is given by the angular

position of the particle along the path.

In the simplest case of two particles that move along circular paths under the same constant force, the particles retain their initial phase difference and do not synchronize or phase lock [27]. Synchronization can be achieved by allowing the radius of the path to vary and relax to a preferred value through a harmonic restoring force [24, 28]. In this case, the differential equation governing their difference in phase reduces to Adler's equation [29], which originated from describing the relative phase of two coupled oscillators. Adler's equation admits two solutions corresponding to in-phase and anti-phase oscillations. Depending on the sign of the coupling parameter, one of these oscillations will be stable, while the other will be unstable. Other modifications of the basic circular-path model, such as allowing for the forcing on the particle to vary with angular position [30], can also yield Adler-like dynamics. These dynamics are found for particles moving along a straight path and driven by a geometrically switching force [31], as well as for models constructed from the principle component analysis of *Chlamydamonas* flagellar movement data [32]. In fact, the stochastically-forced Adler's equation has been used [10] to describe the coupled motion of *Chlamydomonas* flagella, where the anti-phase breast stroke is stable and in-phase undulations are unstable. The stochastic forcing allows for temporary departure anti-phase beating during which time in-phase undulations can be observed.

While basic models have lead the way in studying cilia coordination at larger scale [28, 33], including the onset [24, 25] of metachronal waves, their versatility has also allowed for the exploration of other physical mechanisms present in flagellar motion, such as basal coupling [34, 35]. These mechanisms result in a departure from the standard Adler's equation with the emergence of bistability of the in-phase and anti-phase oscillations for a range of parameter values. Bistable, as well as metastable, states are also obtained [30] when the particles move along elliptical paths under a variable force or along straight paths with geometric switching and cycle-dependent drag variations [36]. Regions of bistability have also been observed in more detailed computational models. Guo *et al.* [36] simulated two flexible filaments attached to a planar surface that were driven by torques at their bases that change direction once a critical angle between the filament base and the surface normal has been achieved. Base actuation, though not representative of cilia and flagella which are instead actuated along their lengths, provides a simple way to explore filament synchronisation. Additionally, base actuation is a potential mechanism for powering the motion of artificial microswimmers

that utilise flexible filaments. Through a series of initial value problems, they showed that for a certain range of base torque magnitude and filament separations the final state can be in-phase or anti-phase, depending on the initial condition of the system. There are different conventions adopted in the literature leading to opposite definitions of anti-phase and in-phase synchronisation. In this paper, as in [36], in-phase refers to the case where the difference in the angles between the filament bases and the surface normal is zero, i.e. $\theta_2(t) - \theta_1(t) = 0$. For studies involving *Chlamydomonas*, for example [37], this is instead referred to as anti-phase and the commonly observed breast-stroke is said to be in-phase.

In this work, we aim to build upon the results established in [36] and explore in more detail the bifurcations encountered when the in-phase and anti-phase oscillations become bistable. In particular, utilizing methods from computational dynamical systems along with the computational methodology developed in [38], we compile the bifurcation diagram for a fixed filament separation, computing the unstable branch in the bistable region that connects with the in-phase branch through a sub-critical pitchfork bifurcation and merges with the upper stable branch through a saddle-node bifurcation. The upper branch itself connects to the anti-phase one through a super-critical pitchfork bifurcation. We characterize each of the states using the phase portrait of the angles at the filament bases. We show how the bifurcation diagram can be replicated through an Adler-like phenomenological model which incorporates the bistable region and appropriate bifurcations through a Duffing-like term. Using the bifurcation points from the bifurcation diagram for the filament system, the model parameters can be tuned, allowing for a quantitative recreation of the original bifurcation diagram.

II.   SIMULATION AND METHODS

We consider two filaments of length l and cross-section radius a. The filaments are tethered to a rigid planar surface and have base separation distance, B, as sketched in Fig. 1. The filaments have bending modulus K_B, and are immersed in a surrounding fluid of viscosity η. Here, the surface-parallel and normal directions are denoted by x and y, and the corresponding unit vectors in these directions are $\hat{\boldsymbol{x}}$ and $\hat{\boldsymbol{y}}$, respectively.
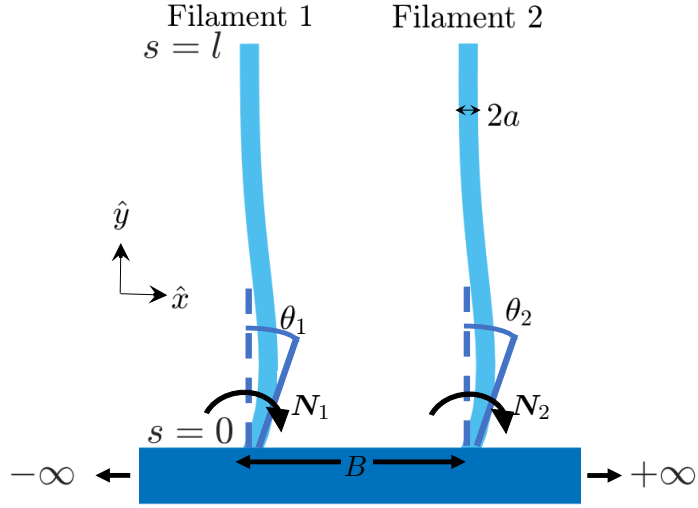
FIG. 1: Schematic diagram for the filament system indicating the arclength $s \in [0, l]$, diameter $2a$, base torques $\boldsymbol{N}_i$, base angles θ_i and separation distance B.

A. Filament model

To compute the motion of the filaments, we utilize the model and numerical methods described and developed in [38], which, for clarity, we summarize here in the context of a single filament. The filament centerline is parameterized by arclength s, such that the position of a point on the centerline at time t is given by $\boldsymbol{Y}(s,t)$. At each point along the filament, we assign a unit vector $\hat{\boldsymbol{t}}(s,t)$ that is constrained to be tangent to the centerline through $\partial \boldsymbol{Y}/\partial s = \hat{\boldsymbol{t}}$. The force and moment balances along the filament are given by

$$\frac{\partial \boldsymbol{\Lambda}}{\partial s} + \boldsymbol{f} = 0, \tag{1}$$

$$\frac{\partial \boldsymbol{M}}{\partial s} + \hat{\boldsymbol{t}} \times \boldsymbol{\Lambda} + \boldsymbol{\tau} = 0, \tag{2}$$

where $\boldsymbol{f}(s,t)$ and $\boldsymbol{\tau}(s,t)$ are the viscous forces and torques per unit length that arise due to the motion of the filament through the surrounding fluid, while $\boldsymbol{\Lambda}(s,t)$ and $\boldsymbol{M}(s,t)$ are the internal force and moment, respectively, on the cross-section of the filament. The internal force arises due to the constraint on $\hat{\boldsymbol{t}}$ and $\boldsymbol{Y}$. The internal moment is related to the curvature, $\boldsymbol{\kappa}(s,t) = \hat{\boldsymbol{t}} \times \partial\hat{\boldsymbol{t}}/\partial s$, through $\boldsymbol{M} = K_B \boldsymbol{\kappa}$.

Along with these balances, at $s = l$, we will have the free-end condition, $\boldsymbol{\Lambda}(l,t) = 0$ and $\boldsymbol{M}(l,t) = 0$, while at $s = 0$, the position of the filament is fixed and $\boldsymbol{M}(0,t) + \boldsymbol{N} = 0$, where

6

N is an applied torque that gives rise to filament motion. Following [36], the base torque is given by $N = \alpha(t)N_0\hat{z}$, where N_0 is the torque magnitude and α is the switching parameter that controls the direction of the driving torque. The value of $\alpha(t)$ varies in time and unlike [36], we allow for it to vary continuously from ± 1 to ∓ 1 over at short time τ_α when the absolute value of the angle, θ, between $\hat{t}(0,t)$ and $\hat{y}$ exceeds the critical angle Θ. Allowing $\alpha(t)$ to vary continuously with time is important to ensure convergence of our implicit time integration scheme. Specifically, if the time at which $|\theta| = \Theta$ is $t = t_\Theta$, then α obeys

$$\alpha(t) = \pm \tanh\left[4\left(\frac{2(t - t_\Theta) - T_\alpha}{\tau_\alpha}\right)\right],\tag{3}$$

for $t \in [t_\Theta, t_\Theta + T_\alpha]$, where T_α sets the timescale over which α changes from ± 1 to ∓ 1.

To compute its motion, the filament is discretized into N segments of length ΔL. The position and orientation vector of segment n are denoted by Y_n and $\hat{t}_n$, respectively. Second-order central differencing is applied to the force and moment balances, Eqs. (1) and (2), to yield

$$\frac{\Lambda_{n+1/2} - \Lambda_{n-1/2}}{\Delta L} + f_n = 0,\tag{4}$$

$$\frac{M_{n+1/2} - M_{n-1/2}}{\Delta L} + \frac{1}{2}\hat{t}_n \times \left(\Lambda_{n+1/2} + \Lambda_{n-1/2}\right) + \tau_n = 0,\tag{5}$$

for segment n where $M_{n+1/2} = K_B\hat{t}_n \times (\hat{t}_{n+1} - \hat{t}_n)/\Delta L$ and $\Lambda_{n+1/2}$ are Lagrange multipliers determined as part of the time integration in order to satisfy the discrete kinematic constraint

$$Y_{n+1} - Y_n - \frac{\Delta L}{2}\left(\hat{t}_n + \hat{t}_{n+1}\right) = 0\tag{6}$$

imposed on segment motion. Multiplying Eqs. (4) and (5) by ΔL produces the force and torque balances on the segments which we express as

$$F_n^C - F_n^H = 0,$$
$$T_n^E + T_n^C - T_n^H = 0,\tag{7}$$

where $F_n^C = \Lambda_{n+1/2} - \Lambda_{n-1/2}$, $T_n^C = (\Delta L/2)\hat{t}_n \times \left(\Lambda_{n+1/2} + \Lambda_{n-1/2}\right)$, and $T_n^E = M_{n+1/2} - M_{n-1/2}$, while F_n^H and T_n^H describe the force and torque segment n exerts on the surrounding fluid. These equations establish the following low Reynolds number mobility problem for segment motion

$$\begin{pmatrix} V \\ \Omega \end{pmatrix} = M \begin{pmatrix} F^H \\ T^H \end{pmatrix}.\tag{8}$$

where for fully 3D motion, $\boldsymbol{V}^\top = (\boldsymbol{V}_1^\top, \ldots, \boldsymbol{V}_N^\top)$ is the $3N \times 1$ vector containing all segment velocity components, while vector $\boldsymbol{\Omega}$ contains all angular velocity components. $\boldsymbol{F}^H$ and $\boldsymbol{T}^H$ are $3N \times 1$ vectors of the forces and torques, respectively, that the segments exert on the fluid as given by Eq. (7). The matrix $\boldsymbol{M}$ is a $6N \times 6N$ mobility matrix, which in our simulations is given by the pairwise Rotne-Prager-Yamakawa (RPY) tensor that accounts for the presence of the no-slip boundary [39]. The hydrodynamic radius of the segments is taken to be the filament cross-sectional radius, a, which is related to the segment length through $a = \Delta L/2.2$. A quantitative comparison between the RPY approximation and numerical solutions to the boundary integral equations [40] in the case of rigid straight filaments in unbounded fluid is provided in [38]. There, the maximum relative errors in the segment forces were found to be approximately 4%.

With $\boldsymbol{V}$ and $\boldsymbol{\Omega}$ given by Eq. (8), the segment positions and orientations that satisfy the constraints, as well as the values of $\boldsymbol{\Lambda}_{n+1/2}$, are updated by integrating in time the differential-algebraic system

$$\frac{d\boldsymbol{Y}_n}{dt} = \boldsymbol{V}_n,$$
$$\frac{d\hat{\boldsymbol{t}}_n}{dt} = \boldsymbol{\Omega}_n \times \hat{\boldsymbol{t}}_n,$$
$$\boldsymbol{Y}_{n+1} - \boldsymbol{Y}_n - \frac{\Delta L}{2}\left(\hat{\boldsymbol{t}}_n + \hat{\boldsymbol{t}}_{n+1}\right) = 0. \tag{9}$$

In our simulations, we apply the implicit second-order backward difference time (BDF) scheme to integrate Eq. (9) numerically. After applying BDF, we are left with a nonlinear system of equations whose solution is the updated values of the positions, orientations and Lagrange multipliers. We solve the nonlinear system iteratively using Broyden's method. For more details about the implementation of this approach, the reader is referred to [38], where a complete description and study of the method can be found.

B. Simulating a filament pair

The model and methods described above readily extend to the case of two such filaments that interact through the surrounding fluid. First, the force and moment balances, Eqs. (1) and (2), are considered for each filament. The base of filament 1 is fixed to the surface at the origin, while the base of filament 2 is tethered at $B\hat{\boldsymbol{x}}$. Additionally, driving the

motion of filament 1 is the applied base torque, $\boldsymbol{N}_1 = \alpha_1(t)N_0\hat{\boldsymbol{z}}$, and correspondingly for filament 2 we have $\boldsymbol{N}_2 = \alpha_2(t)N_0\hat{\boldsymbol{z}}$. The values of α_1 and α_2 follow the switching mechanism described above and are determined separately for each filament. Both filaments are subject to free-end conditions.

The filaments are each discretized into N segments to give a total of $2N$ segments. To allow for interactions between the filaments due to the surrounding fluid, the segment force and torque balances, Eq. (7), for each filament are coupled by extending the low Reynolds number mobility problem, Eq. (2), to the full system of $2N$ segments and allowing all segments from both filaments to interact via the RPY tensor. This yields the velocity and angular velocity for each segment, allowing for the position and orientation of the segments to be updated by integrating Eq. (9) using the same methods as in the case of a single filament.

C.   Non-dimensionalization and simulation parameters

All quantities presented from here on are nondimensional. Specifically, we nondimensionalize distances by the filament length, l, forces by the characteristic bending force, K_B/l^2, and time by the characteristic relaxation time $\eta l^4/K_B$. As presented in [36], typical dimensional values of these parameters are $l = 20\mu m$, $\eta = 10^{-3}$Pas, and $K_B = 800$pNμm^2. In particular, we explore how the steady oscillations and their stability vary with the nondimensional separation distance, $b = B/l$, and nondimensional base torque magnitude, $M_b = N_0 l/K_B$.

For all cases, the filaments are discretized into $N = 19$ segments, giving the filament cross-sectional radius, $a = 0.024$. The torque transition time is set to $\tau_\alpha = T_\alpha/(\eta l^4/K_B) = 1.1 \times 10^{-5}$. The time-step size is $\Delta t = 10^{-6}$ and simulations are run for $t \in [0, T_{tot}]$ with $T_{tot} = 6$. The simulations are performed over the range of dimensionless base torques $M_b = 2.5 - 10$ and for separation distances $b = 0.25 - 3$. We note that for this range of M_b, the filament period of oscillation is typically $T \lesssim 0.04$ and approximately inversely proportional to M_b. Thus, our simulations are run to times of at least $150T$ and we can be reasonably confident that each simulation has reached its asymptotically stable steady oscillation.

III. RESULTS

We begin by considering different initial value problems over the range of b and M_b indicated above and quantify the synchrony of the system at the final time. To measure synchrony, we introduce the synchrony parameter,

$$Q(t_s) = -\frac{1}{t_e - t_s} \int_{t_s}^{t_e} \alpha_1(t)\alpha_2(t)\mathrm{d}t, \tag{10}$$

adapted from [31]. Here, t_s and t_e are the times corresponding to the start and end of the $\alpha_1\alpha_2$ oscillation period. Given the definition of Q in Eq. (10), $Q = 1$ implies that the filaments' beats are completely anti-phase, whereas $Q = -1$ means that the filaments' beats are perfectly in-phase. Based on this convention, the term in-phase refers to case where the filaments undulate, while anti-phase refers to the case of the breast stroke. Further to this, we measure the instantaneous phase difference between the two filaments

$$\Delta\phi(t) = \phi_2(t) - \phi_1(t), \tag{11a}$$

where, following [36], the phase of each filament is given by

$$\phi_i(t) = \frac{\Theta + \alpha_i(t)\theta_i(t)}{4\Theta} + \frac{1 - \alpha_i(t)}{4}, \tag{11b}$$

where $\Theta = \pm0.15\pi$ is the switching angle. For $\theta_i \in [-\Theta, \Theta]$, ϕ_i is a monotonic function varying in the range of $\phi \in [0, 1]$. In particular, for $\phi_i \in [0, 0.5]$, $\alpha_i = 1$, and for $\phi_i \in [0.5, 1]$, $\alpha_i = -1$.

A. Synchronization states

The simulations are run with two different initial conditions. In both cases, the filaments are straight, while imposing: 1) $\phi_1(t = 0) = 0.25$ and $\phi_2(t = 0) = 0.74$ ($\Delta\phi(0) = \phi_2(0) - \phi_1(0) = 0.49$); 2) $\phi_1(t = 0) = 0.25$ and $\phi_2(t = 0) = 0.26$ ($\Delta\phi(0) = 0.01$), corresponding to perturbations from the anti-phase and in-phase states, respectively. The resulting filament dynamics for $M_b = 7$ are shown in Fig. 2, with Fig. 2a showing the anti-phase state and Fig. 2d providing the in-phase state. Figs. 3(a) and 3(b) show the final values of Q obtained for the two different initial conditions for base torques $3 \leq M_b \leq 10$ and filament separations $0.25 \leq b \leq 3$. Here, we note that, for $M_b \lesssim 3$ and $b \lesssim 0.25$, each filament exhibits
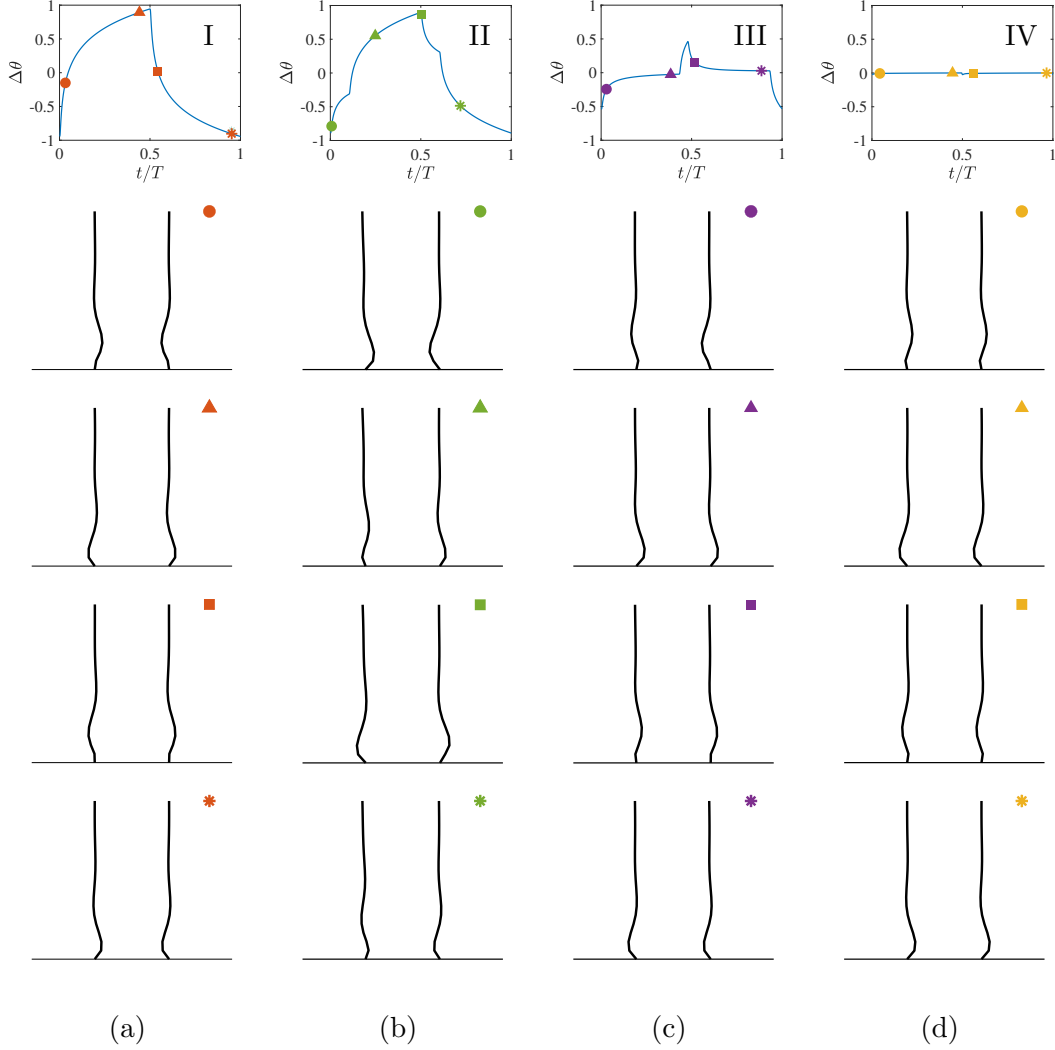
10

FIG. 2: Filament dynamics over one beat period for $M_b = 7$ with (a) Anti-phase oscillations (Branch I), (b) Stable, phase-shifted oscillations (Branch II), (c) Unstable, phase-shifted oscillations (Branch III), and (d) In-phase oscillations (Branch IV). The top panels in each figure show the difference base angles, $\Delta\theta = \theta_2 - \theta_1$, over one period. The symbols correspond to the time points that the filaments are shown.

.

significant motion at its free-end and the filaments collide. As observed filament shapes are broadly similar to those found for isolated cases with the same value of M_b, we conclude that filament shapes are largely unaffected by the hydrodynamic interactions between the filaments. Accordingly, the filament shapes are largely independent of whether the filaments are in the in-phase or anti-phase state. This property can be seen Fig. 2 by comparing
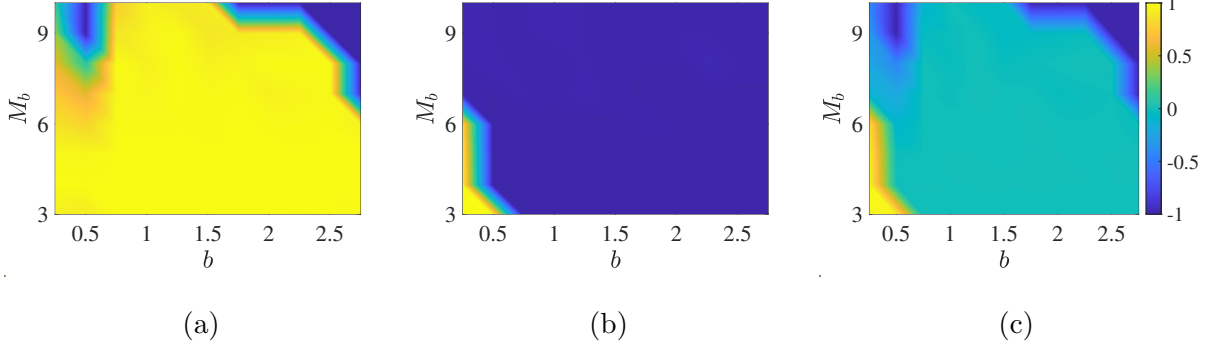
FIG. 3: The synchrony parameter $Q \in [-1, 1]$ of the asymptotic state in the $M_b - b$ plane: (a) $\Delta\phi = 0.49$; (b) $\Delta\phi = 0.01$. $Q = 1$ corresponds to anti-phase beating, and $Q = -1$ corresponds to in-phase beating. In (c), the contours show $\Delta Q = (Q_{0.49} + Q_{0.01})/2 \in [-1, 1]$, where the subscript indicates the value of $\Delta\phi$ for which Q was computed. $\Delta Q \approx 0$ in (c) indicates bistability.

.

the filament shapes for the different states. The key parameter, therefore, governing the filament shape over time is M_b, which also controls directly the oscillation frequency.

At sufficiently low values of b ($b < 0.75$) and regardless of the initial conditions, the filament pair exhibits asymptotically stable anti-phase synchrony ($Q \simeq 1$) for $M_b \lesssim 3.5$. For the initial condition with $\Delta\phi = 0.49$, the asymptotically stable state transitions from the anti-phase to in-phase synchrony for $7 \lesssim M_b \lesssim 9$ (Fig. 3a). A similar change occurs for the $\Delta\phi = 0.01$ initial condition, but it at a lower value of M_b. This suggests the existence of bistability for a range of M_b where both in-phase and anti-phase synchrony states are stable. This bistable region is also shown in Fig. 3(c) by the region of $\Delta Q = (Q_{0.49} + Q_{0.01})/2 \simeq 0$, where $Q_{0.49}$ and $Q_{0.01}$ are the synchrony parameters Q of the asymptotic states for $\Delta\phi = 0.49$ and $\Delta\phi = 0.01$, respectively. As b increases from $b = 0.25$ to $b = 1$, the range of M_b which yields bistability widens. However, further increasing b beyond $b \simeq 1.25$ reduces the range of M_b for which bistability is observed, with the upper limit decreasing with b (i.e. the blue region in Fig. 3).

Regions of stable in-phase oscillations and stable anti-phase oscillations separated by a region of their bistability, were previously found [36] for this system for similar values of b, but at a much lower and more narrow range of base torques, $2 \lesssim M_b \lesssim 2.5$. We suspect that these quantitative differences are due differences in models for the hydrodynamic mobility of the
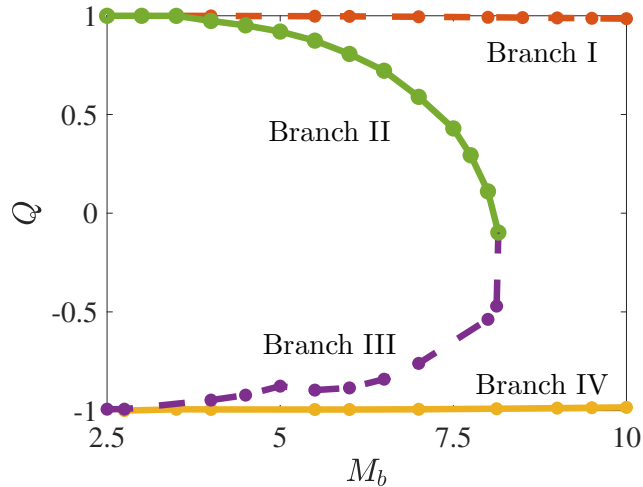
12

FIG. 4: Bifurcation of synchronized states represented by Q with $M_b \in [2.5, 10]$ and $b = 0.5$. Here, the solid and dashed lines indicate stable and unstable states, respectively, and the markers indicate the simulation data.

segments. To compute segment mobility, Guo *et al.* [36] employed regularized Stokeslets with a point-wise evaluation of the flow at the segment centers. This results in higher diagonal entries of the filament mobility matrix, hence a lower segment drag coefficient, as compared to our RPY-based approach and, therefore, for a given value of M_b, the regularized Stokeslet model will oscillate at a higher frequency. This, in turn, results in the Sperm number, the ratio of viscous to elastic forces, being larger for a regularized Stokeslet filament, allowing it to bend more at a fixed value of M_b. This aspect allowed [36] to investigate very low values of M_b and b where they observe a second region of bistability, while in our case, the filaments undergo rigid body motion and collide.

B. Bifurcation and stability analysis

To explore the nature of bistability in more detail, we perform a computational bifurcation analysis of the filament system. As such an analysis typically requires many repeated simulations, we focus our attention on the case of $b = 0.5$ where multiple bifurcations and bistability are observed (see Fig. 3) over the range of M_b that we consider.

Fig. 4 shows the bifurcation diagram for the steady oscillatory states represented by Q, and where M_b is the bifurcation parameter. The stable oscillatory states (Branches II and

IV) are computed by fixing M_b and allowing the simulation to reach a steady oscillation for a specified initial condition. To carefully track how these states evolve along the bifurcation curves, a numerical continuation is performed by imposing the steady oscillation for M_b as the initial condition of a simulation with $M_b + \Delta M_b$. We also used numerical continuation to obtain the unstable Branch I ($Q \simeq 1$) up to $M_b = 10$ by carefully controlling each simulation before the instability develops. This indicates also that there is a relatively small growth rate along the unstable eigendirection associated with this state. We obtained identical results for the Branch I states by performing simulations where mirror symmetry in filament motion is imposed, in which case Branch I is a stable equilibrium. Finally, we calculate the unstable Branch III placed between Branches II and IV for $2.75 \lesssim M_b \lesssim 8$ using the bisection algorithm outlined in [41].

To examine the stability of Branch I, we first obtained the solutions corresponding to this branch from the simulations with imposed mirror symmetry. Then, for each M_b, we run a simulation where the initial conditions are set by perturbing a snapshot taken from the corresponding Branch I solution. The perturbation is introduced by rotating filament 2 by 0.78 degrees. A careful observation of the perturbation evolution suggests that the initial form of the instability arises primarily with an increase of the oscillation period. To examine the evolution of the perturbation further, we first compute the piecewise constant function, $\gamma(t)$ that increases by one each time α_1 changes sign. Using this function, we then compute

$$\Gamma(t_s) = \frac{1}{t_e - t_s} \int_{t_s}^{t_e} |\gamma(t) - \gamma_{AP}(t)| dt, \tag{12}$$

where $\gamma_{AP}(t)$ is the piecewise function computed from the Branch I solution. The times t_e and t_s are defined above in Section II A and are determined also from the Branch I solution. From its definition, we see that $\Gamma(t)$ will be constant in time if the oscillations in the two simulations have the same period but a different phase and will increase monotonically if the periods also differ.

The different branches and the bifurcations leading to these states are shown in Fig. 4 and summarised below. Their phase portraits on the $\theta_1 - \theta_2$ plane are also shown in Fig. 5.

1. Branch I: This branch is formed along $Q = 1$, indicating anti-phase synchrony for this state. The phase portrait in the $\theta_1 - \theta_2$ plane shows that the state forms a limit cycle and its shape nearly overlaps with the straight line $\theta_1 + \theta_2 = 0$ (Fig. 5a).
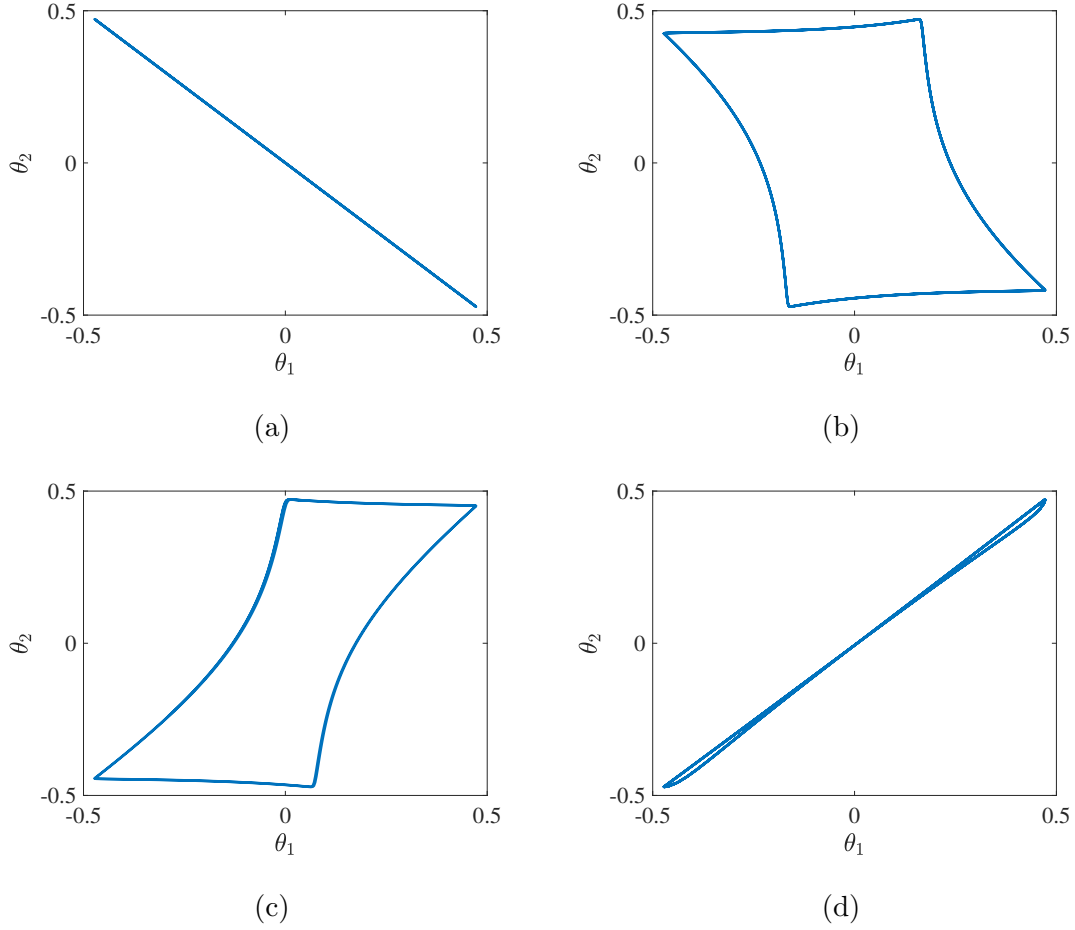
14

FIG. 5: Phase portrait in θ_1-θ_2 space for the synchronized states for $M_b = 7$: (a) Branch I (anti-phase oscillations); (b) Branch II (stable, phase-shifted oscillations); (c) Branch III (unstable phase-shifted oscillations corresponding to the edge state); (d) Branch IV (in-phase oscillation). Filament dynamics corresponding to these cases are shown in Fig. 2.

However, for $M_b \gtrsim 2.5$, this branch is unstable as perturbations to this state exhibit an initial exponential growth in time (see the dashed lines is Fig. 6(a). For $M_b = 2.5$, $\Gamma(t)$ increases rapidly and attains a constant value, indicating that at long times the filaments oscillate with the same period as the anti-phase state. The phase portrait for this case, Fig. 6(b), shows the oscillations attaining a limit cycle close to, but not precisely, that of the anti-phase state. These observations suggest that $M_b = 2.5$ is very close to the bifurcation point. For $M_b = 6$, we see that Γ continues to grow even after its initial exponential increase as the solution moves towards Branch II and attains a different period of oscillation. The evolution of the limit cycle in the $\theta_1 - \theta_2$
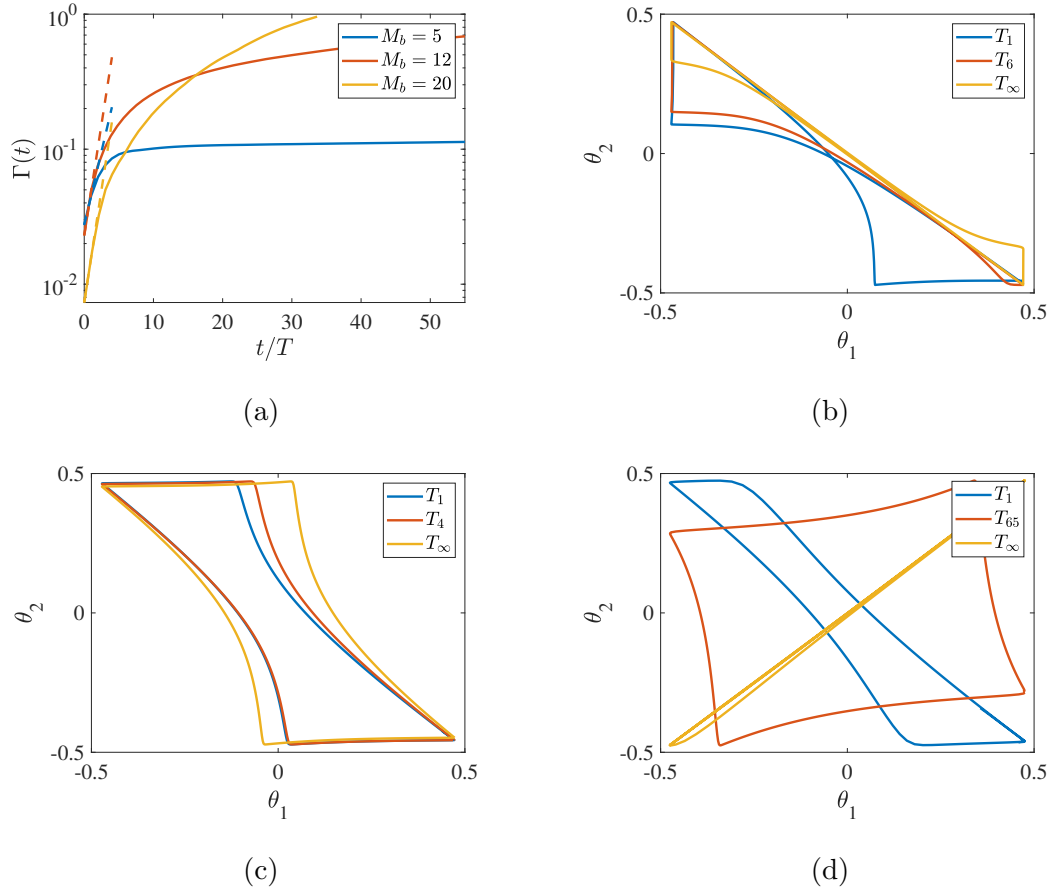
FIG. 6: Stability of Branch I (anti-phase oscillations): (a) $\Gamma(t)$ for cases $M_b = 2.5, 6$ and 10. Phase portraits for (b) $M_b = 2.5$, (c) $M_b = 6$, and (d) $M_b = 10$. The different colored lines show trajectories over one period beginning at period T_i as indicated in the legend. In each case T_∞ shows the limit cycle at once the oscillations are steady.

plane for this case is shown in Fig. 6(c). For $M_b = 10$, we observe a more dramatic increase in $\Gamma(t)$ with time, while the phase portrait (Fig. 6(d)) illustrates that the solution eventually achieves in-phase oscillations and reaches Branch IV.

2. Branch II: This branch appears to emerge via a supercritical pitchfork bifurcation at a value just below $M_b < 2.5$, as the phase portraits of Branch I (Fig. 5a) and Branch II (Fig. 6b) are very similar at $M_b = 2.5$. Close to the bifurcation point, this branch exhibits nearly-perfect anti-phase synchrony, but the value of Q evolves non-trivially along the bifurcation curve. In the phase portrait (Fig. 5b), this branch forms a limit cycle roughly aligned with the line $\theta_1 + \theta_2 = 0$. Following the branch as M_b increases,

Q decreases while the interior area of the limit cycle in the phase portrait increases (Fig. 5b). The interior area of the limit cycle reaches its maximum when $Q \approx 0$ and $M_b \approx 8.15$. Here, a saddle-node point is formed and this stable branch ceases to exist (Fig. 4).

3. Branch III (edge state): Along with Branch II, this branch emerges from a saddle-node bifurcation at $M_b \simeq 8.15$. This branch is unstable and is situated between Branch II and Branch IV, which are both stable. Accordingly, in state space, this branch should sit on the boundary of the basin of attraction for Branch II and that for Branch IV. We can therefore compute this state using the bisection algorithm from Skufca *et al.* [41]. Specifically, we first consider two initial conditions, one of which corresponds to a solution that eventually reaches Branch II, while the other gives a solution that approaches Branch IV. The initial conditions are repeatedly bisected to obtain two solutions whose initial difference in Q is 10^{-8} even though they eventually approach the different states given by Branches II and IV. The time traces of Q corresponding to these two solutions are shown in Fig. 7 (blue and red lines for $0 \leq t \lesssim 0.01$). They share nearly the same value of Q (black line in Fig. 7) until at $t \approx 0.01$ the Q values begin to diverge from each other. At this time, we perform another bisection of the solution to obtain an approximation of the edge state for $0.01 \lesssim t \lesssim 0.03$. By repeating this procedure as t increases, we ensure that the solution remains on the boundary between the state-space basins of attraction of Branches II and IV and obtain the unstable solutions that form Branch III.

As shown in Fig. 4, this branch is connected to Branches II and IV at $M_b \approx 2.5$ and $M_b \approx 8.15$ (dashed purple line), respectively. The phase portrait of this branch shows a limit cycle in the θ_1-θ_2 plane (Fig. 5c) similar in shape to that obtained for Branch II, however here, we see that the limit cycle is aligned instead with $\theta_1 = \theta_2$. Moving along Branch III in the direction of decreasing M_b, one observes that the interior area of the limit cycle gradually decreases until it collapses to the line $\theta_1 = \theta_2$ when it intersects Branch IV and one obtains a state with near-perfect in-phase synchrony.

4. Branch IV: On this branch, the filaments exhibit in-phase synchrony with $Q \simeq -1$. The phase portrait in Fig. 5(d) confirms this as the limit cycle is very close to $\theta_1 = \theta_2$. This branch is connected to Branch III through a subcritical pitchfork bifurcation
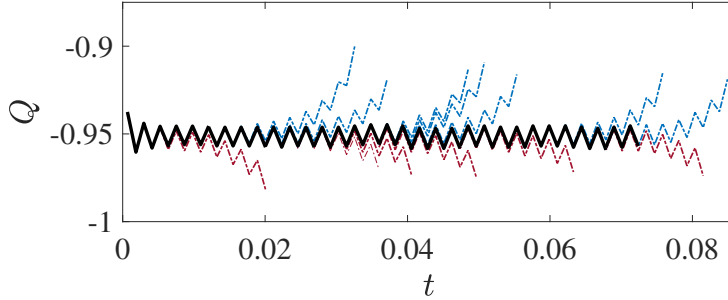
FIG. 7: $Q(t)$ for the edge state (solid black line) corresponding Branch III for $M_b = 4$. The dash-dotted blue lines indicate the trajectories that approach Branch II when performing the bisection, while the dash-dotted red lines show the trajectories that move toward Branch IV.

point at $M_b \approx 2.5$. Simulations with M_b below this value that are initiated close to in-phase synchrony are found to transition to Branch I.

As done in previous studies of synchronisation due to hydrodynamic coupling, it is often useful to relate the observed states and their stability back to those exhibited by classical phenomenological models of coupled oscillators. For many such systems, it has been found [10, 16] that the steady oscillations and their stability can be described by the classical Adler's equation [29] which admits steady in-phase and anti-phase oscillations, the stabilities of which depend on the sign of the coupling parameter appearing in the equation. The bifurcation diagram shown above and, in particular, the presence of bistability indicate that the filament system exhibits dynamics richer than those found for Adler's equation. To resolve this, we propose a modification of Adler's equation through the introduction of a 'Duffing'-like interaction term to capture the observed bistability and various bifurcations.

To do this, we first consider a simple model equation for the phase of each oscillator:

$$\dot{\psi}_1(t) = \omega_1 - \frac{\sigma}{2}\sin(\psi_1(t) - \psi_2(t)) + \frac{\lambda}{2}\sin^3(\psi_1(t) - \psi_2(t)), \tag{13}$$

$$\dot{\psi}_2(t) = \omega_2 - \frac{\sigma}{2}\sin(\psi_2(t) - \psi_1(t)) + \frac{\lambda}{2}\sin^3(\psi_2(t) - \psi_1(t)),$$

where $\psi_i(t)$ and ω_i are the phase and intrinsic frequency of, respectively, of oscillator i. Here, the first nonlinear term with coefficient σ in (13) is the coupling term found in the classical Adler's equation [29]. The second nonlinear term with coefficient λ is the term newly introduced in the present study. We will see that addition of this term leads to the

18

bifurcation behavior of the synchronized states consistent with that observed in the full filament model. We note that the bifurcation behaviour is seen only for small filament separations, indicating that the nonlinear term describes phenomenologically the near-field ($b < 1$) hydrodynamic interactions. The equation for the phase difference between the two oscillators, $\Delta(t) = \psi_1 - \psi_2$, is then given by

$$\dot{\Delta}(t) = \delta\omega - \sigma\sin(\Delta) + \lambda\sin^3(\Delta), \tag{14}$$

where $\delta\omega = \omega_1 - \omega_2$. The model in (13) may be made directly comparable to the full filament model if we take $\theta_i = 2\Theta\psi_i/\pi$ for $\psi_i \in [-\pi/2, \pi/2)$ and $\theta_i = 2\Theta(\pi - \psi_i)/\pi$ for $\psi_i \in [\pi/2, 3\pi/2)$. In this case, (11b) and (13) will then also admit a direct relation between the synchrony parameter Q in (10) and a steady Δ, namely $Q = -1 + 2\Delta/\pi$.

If, like our filament model, the two oscillators have identical intrinsic frequencies (i.e. $\delta\omega = 0$), Eq. (14) yields the steady states that satisfy

$$\sin(\Delta) = 0 \quad \text{and} \quad \sin^2(\Delta) = \frac{\sigma}{\lambda}. \tag{15}$$

For $\Delta \in [0, \pi]$, the first equation in Eq. (15) has two solutions $\Delta(\equiv \Delta_1) = 0$ and $\Delta(\equiv \Delta_2) = \pi$, which would represent the in-phase ($Q = -1$) and anti-phase synchronized states ($Q = 1$), respectively. Similarly, the second equation has two solutions $\Delta(\equiv \Delta_3) = \sin^{-1}(\sigma/\lambda)$ for $\Delta_3 \in [0, \pi/2]$ and $\Delta(\equiv \Delta_4) = \pi - \sin^{-1}(\sigma/\lambda)$ for $\Delta_4 \in [\pi/2, \pi]$. These two solutions only exist for $0 \leq \sigma/\lambda \leq 1$, and they originate due to the newly-introduced cubic interaction term in (14).

To examine the stability these four solutions, we consider a small perturbation around each equilibrium solution $\Delta_k + \epsilon\tilde{\Delta}$ with $\epsilon \ll 1$ where $k = 1, 2, 3, 4$. When $k = 1, 2$, the linearized equation for the perturbation is

$$\dot{\tilde{\Delta}}(t) = -\sigma\cos(\Delta_k)\tilde{\Delta}, \tag{16a}$$

indicating that Δ_1 and Δ_2 are stable and unstable if $\sigma > 0$, and vice versa. Similarly, for $k = 3, 4$, we have,

$$\dot{\tilde{\Delta}}(t) = 2\sigma\cos(\Delta_k)\tilde{\Delta}, \tag{16b}$$

and therefore, Δ_3 and Δ_4 are unstable and stable if $\sigma > 0$, and vice versa.

From Eqs. (15) and (16), it is evident that the parameter σ controls the existence and stability of the four equilibrium solutions, whereas λ only determines their existence.
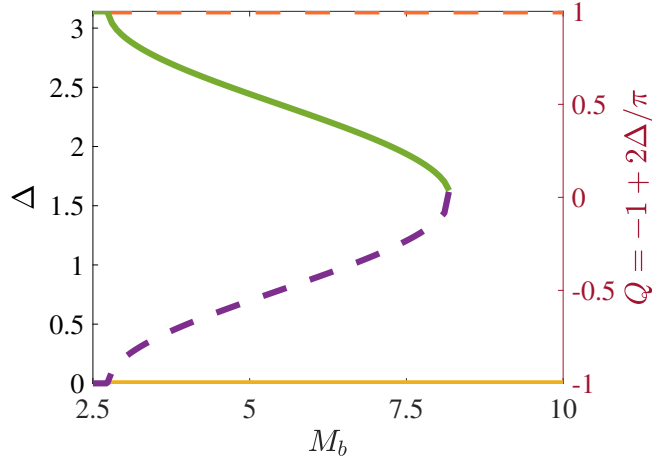
FIG. 8: Bifurcation diagram of the modified Adler's model for the pitchfork bifurcation
base torque $M_{b,PF} = 2.75$ and saddle-node bifurcation value $M_{b,SN} = 8.2$. $\Delta = 0$ and
$\Delta = \pi$ correspond to in-phase and anti-phase synchronization respectively. Here,
$Q = -1 + 2\Delta/\pi$ (see main text).

Therefore, σ alone controls the bifurcations of Eq. (14) and functions as M_b did in the
filament model. Furthermore, if $\sigma = 0$, $\Delta_1 = \Delta_3 = 0$ and the two stationary solutions
are neutrally stable. Also, for $\sigma < 0$, Δ_3 does not exist, indicating that Δ_3 emerges via
a pitchfork bifurcation at $\sigma = 0$. The same pitchfork bifurcation appears for Δ_2 and Δ_4.
When $\sigma = 0$, $\Delta_2 = \Delta_4 = \pi$ with neutral stability, and Δ_4 does not exist for $\sigma < 0$. Finally,
if $\sigma = \lambda$, $\Delta_3 = \Delta_4 = \pi/2$ and both solutions are neutrally stable. Also, they do not exist for
$\sigma > \lambda$ and their stability is always opposite, e.g. if one is stable and the other is unstable.
This indicates that a saddle-node bifurcation takes place for Δ_3 and Δ_4 when $\sigma = \lambda$.

By comparing the stabilities and bifurcations of the four solutions with the corresponding
occurrences in the filament model, we can relate σ and λ to M_b and the values of M_b at
which bifurcations occur. First, since the stabilities of Branches I and IV in Fig. 4 are found
to be change at $M_b \approx 2.5$, we will assume that Δ_1 and Δ_2 undergo pitchfork bifurcations
near this value, $M_b = 2.75 (\equiv M_{b,PF})$, say. Second, we observe that all four branches in
Fig. 4 exist for $2.75 \lesssim M_b \lesssim 8.2$, with $M_b \approx 8.2$ corresponding to the saddle-node point for
Branches II and III. Therefore, we will assume that Δ_3 and Δ_4 exist for $2.75 \leq M_b \leq 8.2$
and $\Delta_3 = \Delta_4$ at $M_b = 8.2 (\equiv M_{b,PF})$. We now define

$$\sigma \equiv \beta(M_b - M_{b,PF}) \quad \text{and} \quad \lambda \equiv \beta(M_{b,SN} - M_{b,PF}) \tag{17}$$

20

with $\beta < 0$ controlling the strength of the interaction terms in Eq. (14), as well as the strength of equilibrium state stability.

The bifurcation diagram with parameter values set according to Eq. (17) is shown in Fig. 8. The model yields a qualitatively similar bifurcation behavior. There are two pitchfork bifurcations that occur at $M_b = M_{b,PF}$ for the in-phase and anti-phase synchronized states ($\Delta \in \{0, \pi\}$) respectively. The two intermediate states emerge via these bifurcations and meet at $\Delta = \pi/2$ to form the saddle-node point at $M_b = M_{b,SN}$. It is also worth mentioning that the value of β does not change the bifurcation diagram in Fig. 8 as long as it remains negative – if β is positive, the stable and unstable states in 8 exchange their stability and become unstable and stable states, respectively. Finally, we note that Eq. (17) is not the only way to model the bifurcation of the full filament model. For example, setting $\sigma = \beta(M_b - M_{b,PF})^m$ and $\lambda \equiv \beta(M_{b,SN} - M_{b,PF})^m$ for any odd integer m will yield the same bifurcations as (14). The more general requirements of determining σ and λ are that 1) σ should vary monotonically with the bifurcation parameter while covering both positive and negative real numbers and that 2) λ is set to obtain four equilibrium solutions when $0 \leq \sigma/\lambda \leq 1$. Provided that these conditions on σ and λ are satisfied, the bifurcations observed for the full filament model can be reproduced using the modified Adler's equation.

IV. CONCLUDING REMARKS

In this paper, we studied the synchronization of a pair of filaments that are tethered to a flat surface and driven at their bases by geometrically-switching torques. Exploring the parameter space of filament separation distance and base torque magnitude, we found that the bistability of in-phase and anti-phase oscillations exists for a large region of the parameter space. Fixing the filament separation distance and allowing the base torque to vary, we utilized a variety of techniques, including bisection for edge state classification, to study the bifucations that gave rise to bistability. The beginning of the bistable region coincided with two simultaneous pitchfork bifurcations, a subcritical bifurcation from the in-phase branch and a supercritical one from the anti-phase branch. The bistable region ended at a saddle-point when the unstable solution that bifurcated from the in-phase branch merged with the stable solution that bifurcated from the anti-phase branch. Finally, we showed that the inclusion of additional nonlinear terms in Adler's equation allowed us to reproduce

quantitatively the bifurcation diagram for the filament system.

The similarities between the bifurcation diagram for the filament system and that of the phenomenological model suggest that bistability may be a more generic property of a particular class of mechanically coupled oscillators. In very recent work, Man and Kanso [42] found the same bifurcations occurring for a filament pair where the filaments are driven by a follower force [43, 44] applied to the filaments' distal ends rather than the geometrically switching base torques used here. Despite the actuation being very different, a similar bifurcation diagram emerges. The two, closely-separated flagella of *Chamydomonas* are connected in the basal body via the elastic distal striated fiber [14] and this elastic coupling has been shown [16] to play a key role in flagellar synchronization for *Chamydomonas*. Oscillator models [34, 45] that include elastic basal coupling are also found to exhibit bistability of synchronized states, even in the absence of hydrodynamic interactions [45].

While we note that the model does not correspond directly to *Chamydomonas* flagella and, as a result, we must be careful to draw any direct conclusions, the bistability it exhibits (also highlighted by [45]) does point to a potential gait-switching mechanism that incorporates gait modulation and is consistent with experimental measurements of Ca^{2+} currents. Specifically, the cell may maintain relevant quantities that stimulate flagellar actively in a range where only the anti-phase breast stroke is stable. This corresponds to low M_b in our model. Operating in this regime has the benefit that anti-phase beating would be robust to perturbations as it is the only stable steady state. Modestly increasing activity levels would allow for the continuous modulation of the anti-phase state, just as increasing M_b changes the synchrony parameter along Branch II. A sufficiently large increase in activity, however, would induce a transition to in-phase beating. Due to bistability, activity levels can returned to modest levels and the flagella can maintain in-phase undulation. Finally, when the activity level relaxes back to its very low rest value, beating returns to the anti-phase state.

Generally speaking, this picture is consistent with the calcium ion (Ca^{2+}) currents found [46] to be important to changing flagellar synchrony in *Chlamydomonas* during photoshock where the cell experiences a short, high intensity light pulse. This switching is also found [12] to occur during mechanoshock, where *Chlamydomonas* experiences a sudden, intense mechanical stimulus, and again, Ca^{2+} channels play a fundamental role in this response. Experiments have shown [47] that large changes in Ca^{2+} concentrations cause flagella to

transition from anti-phase breast-stroke to in-phase undulations, while more modest increases lead to modulation of the anti-phase breast-stroke. In the case of photoshock, the light pulse triggers the opening of ion channels, allowing the a large flux of Ca^{2+} into the flagella, inducing the transition from anti-phase breast-stroke to in-phase undulations. After this transition, the Ca^{2+} flux is maintained at a lower level for the 600ms that the flagella perform in-phase undulation. A closer connection, however, will need to be made between the models and the cellular mechanisms at play to test this hypothesis and elucidate more clearly the precise reason for the transition. Further, bistability could potentially be used as mechanism to control the synchronised states of artificial cilia. Such devices would, however, likely need to be driven independently and allow the artificial cilia to switch their beat direction due to the flows generated by their neighbours. Magnetic cilia, such as those developed in [48–50], are driven externally by the same magnetic field. Thus, their dynamics are influenced almost exclusively by the applied field, rather than the interactions with neighbouring cilia, though tuning the magnetic properties of the cilia during device construction can affect the overall collective state [50]. Devices actuated using light, such as in [51], with illumination linked to device geometry, could instead be a potential system to explore the bistability of synchronised states experimentally.

---

[1] I. Gibbons, Cilia and flagella of eukaryotes., The Journal of cell biology **91**, 107s (1981).

[2] E. A. Gaffney, H. Gadêlha, D. Smith, J. Blake, and J. Kirkman-Brown, Mammalian sperm motility: observation and theory, Annual Review of Fluid Mechanics **43**, 501 (2011).

[3] R. E. Goldstein, Green algae as model organisms for biological fluid dynamics, Annual review of fluid mechanics **47**, 343 (2015).

[4] C. Brennen and H. Winet, Fluid mechanics of propulsion by cilia and flagella, Annual Review of Fluid Mechanics **9**, 339 (1977).

[5] D. J. Smith, T. D. Montenegro-Johnson, and S. S. Lopes, Symmetry-breaking cilia-driven flow in embryogenesis, Annual Review of Fluid Mechanics **51**, 105 (2019).

[6] M. A. Sleigh, J. R. Blake, and N. Liron, The propulsion of mucus by cilia, American Review of Respiratory Disease **137**, 726 (1988).

[7] R. Faubel, C. Westendorf, E. Bodenschatz, and G. Eichele, Cilia-based flow network in the brain ventricles, Science **353**, 176 (2016).

[8] E. M. Purcell, Life at low reynolds number, in *Physics and our world: reissue of the proceedings of a symposium in honor of Victor F Weisskopf* (World Scientific, 2014) pp. 47–67.

[9] U. Rüffer and W. Nultsch, High-speed cinematographic analysis of the movement of chlamydomonas, Cell Motility **5**, 251 (1985).

[10] R. E. Goldstein, M. Polin, and I. Tuval, Noise and synchronization in pairs of beating eukaryotic flagella, Phys. Rev. Let. **103**, 168103 (2009).

[11] M. Polin, I. Tuval, K. Drescher, J. P. Gollub, and R. E. Goldstein, Chlamydomonas swims with two "gears" in a eukaryotic version of run-and-tumble locomotion, Science **325**, 487 (2009).

[12] K. Fujiu, Y. Nakayama, A. Yanagisawa, M. Sokabe, and K. Yoshimura, Chlamydomonas cav2 encodes a voltage-dependent calcium channel required for the flagellar waveform conversion, Current Biology **19**, 133 (2009).

[13] K. Y. Wan and R. E. Goldstein, Time irreversibility and criticality in the motility of a flagellate microorganism, Physical review letters **121**, 058103 (2018).

[14] K. Y. Wan, Coordination of eukaryotic cilia and flagella, Essays in biochemistry **62**, 829 (2018).

[15] D. R. Brumley, K. Y. Wan, M. Polin, and R. E. Goldstein, Flagellar synchronization through direct hydrodynamic interactions, Elife **3**, e02750 (2014).

[16] G. Quaranta, M.-E. Aubin-Tam, and D. Tam, Hydrodynamics versus intracellular coupling in the synchronization of eukaryotic flagella, Phys. Rev. Let. **115**, 238101 (2015).

[17] K. Y. Wan and R. E. Goldstein, Coordinated beating of algal flagella is mediated by basal coupling, PNAS **113**, E2784 (2016).

[18] V. F. Geyer, F. Jülicher, J. Howard, and B. M. Friedrich, Cell-body rocking is a dominant mechanism for flagellar synchronization in a swimming alga, Proceedings of the National Academy of Sciences **110**, 18058 (2013).

[19] D. Mondal, R. Adhikari, and P. Sharma, Ciliary oscillations without external friction near the

instability threshold, arXiv preprint arXiv:1904.07783 (2019).

[20] D. B. Hill, V. Swaminathan, A. Estes, J. Cribb, E. T. O'Brien, C. W. Davis, and R. Superfine, Force generation and dynamics of individual cilia under external loading, Biophysical journal **98**, 57 (2010).

[21] J. Elgeti and G. Gompper, Emergence of metachronal waves in cilia arrays, Proceedings of the National Academy of Sciences **110**, 4470 (2013).

[22] J. Han and C. S. Peskin, Spontaneous oscillation and fluid–structure interaction of cilia, Proceedings of the National Academy of Sciences **115**, 4417 (2018).

[23] R. Golestanian, J. M. Yeomans, and N. Uchida, Hydrodynamic synchronization at low reynolds number, Soft Matter **7**, 3074 (2011).

[24] D. R. Brumley, M. Polin, T. J. Pedley, and R. E. Goldstein, Hydrodynamic synchronization and metachronal waves on the surface of the colonial alga volvox carteri, Physical review letters **109**, 268102 (2012).

[25] D. R. Brumley, M. Polin, T. J. Pedley, and R. E. Goldstein, Metachronal waves in the flagellar beating of volvox and their hydrodynamic origin, Journal of the Royal Society Interface **12**, 20141358 (2015).

[26] N. Bruot and P. Cicuta, Realizing the physics of motile cilia synchronization with driven colloids, Ann. Rev. Condensed Matter Phys. **7**, 323 (2016).

[27] P. Lenz and A. Ryskin, Collective effects in ciliar arrays, Physical biology **3**, 285 (2006).

[28] T. Niedermayer, B. Eckhardt, and P. Lenz, Synchronization, phase locking, and metachronal wave formation in ciliary chains, Chaos: An Interdisciplinary Journal of Nonlinear Science **18**, 037128 (2008).

[29] R. Adler, A study of locking phenomena in oscillators, Proc. IRE **34**, 351 (1946).

[30] N. Uchida and R. Golestanian, Hydrodynamic synchronization between objects with cyclic rigid trajectories, Eur. Phys. J. E **35**, 1 (2012).

[31] J. Kotar, M. Leoni, B. Bassetti, M. C. Lagomarsino, and P. Cicuta, Hydrodynamic synchronization of colloidal oscillators, Proc. Nat. Acad. Sciences **107**, 7669 (2010).

[32] G. S. Klindt, C. Ruloff, C. Wagner, and B. M. Friedrich, Load response of the flagellar beat, Physical review letters **117**, 258101 (2016).

[33] N. Uchida and R. Golestanian, Synchronization and collective dynamics in a carpet of microfluidic rotors, Physical review letters **104**, 178103 (2010).

[34] G. S. Klindt, C. Ruloff, C. Wagner, and B. M. Friedrich, In-phase and anti-phase flagellar synchronization by waveform compliance and basal coupling, New J. Physics **19**, 113052 (2017).

[35] Y. Liu, R. Claydon, M. Polin, and D. R. Brumley, Transitions in synchronization states of model cilia through basal-connection coupling, Journal of The Royal Society Interface **15**, 20180450 (2018).

[36] H. Guo, L. Fauci, M. Shelley, and E. Kanso, Bistability in the synchronization of actuated microfilaments, J. Fluid Mech. **836**, 304 (2018).

[37] K. C. Leptos, K. Y. Wan, M. Polin, I. Tuval, A. I. Pesci, and R. E. Goldstein, Antiphase synchronization in a flagellar-dominance mutant of chlamydomonas, Physical review letters **111**, 158101 (2013).

[38] S. F. Schoeller, A. K. Townsend, T. A. Westwood, and E. E. Keaveny, Methods for suspensions of passive and active filaments, arXiv preprint arXiv:1903.12609 (2019).

[39] J. W. Swan and J. F. Brady, Simulation of hydrodynamically interacting particles near a no-slip boundary, Phys.Fluids **19**, 113306 (2007).

[40] E. E. Keaveny and M. J. Shelley, Applying a second-kind boundary integral equation for surface tractions in stokes flow, J. Comp. Phys. **230**, 2141 (2011).

[41] J. D. Skufca, J. A. Yorke, and B. Eckhardt, Edge of chaos in a parallel shear flow, Phys. Rev. Let. **96**, 174101 (2006).

[42] Y. Man and E. Kanso, Multisynchrony in active microfilaments, Physical Review Letters **125**, 148101 (2020).

[43] G. De Canio, E. Lauga, and R. E. Goldstein, Spontaneous oscillations of elastic filaments induced by molecular motors, Journal of The Royal Society Interface **14**, 20170491 (2017).

[44] F. Ling, H. Guo, and E. Kanso, Instability-driven oscillations of elastic microfilaments, Journal of The Royal Society Interface **15**, 20180594 (2018).

[45] H. Guo, Y. Man, K. Y. Wan, and E. Kanso, Intracellular coupling modulates biflagellar synchrony, Journal of the Royal Society Interface **18**, 20200660 (2021).

[46] E.-M. Holland, F.-J. Braun, C. Nonnengässer, H. Harz, and P. Hegemann, The nature of rhodopsin-triggered photocurrents in chlamydomonas. i. kinetics and influence of divalent ions, Biophysical journal **70**, 924 (1996).

[47] G. L. Wheeler, Calcium-dependent signalling processes in chlamydomonas, in *Chlamy-*

domonas: Molecular Genetics and Physiology (Springer, 2017) pp. 233–255.

[48] A. Babataheri, M. Roper, M. Fermigier, and O. Du Roure, Tethered fleximags as artificial cilia, Journal of Fluid Mechanics **678**, 5 (2011).

[49] Y. Wang, Y. Gao, H. Wyss, P. Anderson, and J. den Toonder, Out of the cleanroom, self-assembled magnetic artificial cilia, Lab on a Chip **13**, 3360 (2013).

[50] H. Gu, Q. Boehler, H. Cui, E. Secchi, G. Savorana, C. De Marco, S. Gervasoni, Q. Peyron, T.-Y. Huang, S. Pane, *et al.*, Magnetic cilia carpets with programmable metachronal waves, Nature communications **11**, 1 (2020).

[51] H. Zhang, L. Koens, E. Lauga, A. Mourran, and M. Möller, A light-driven microgel rotor, Small **15**, 1903379 (2019).